

# An evaluation of ice formation in large-eddy simulations of supercooled Arctic stratocumulus using ground-based lidar and cloud radar

B. van Dierenhoven,<sup>1,2</sup> A. M. Fridlind,<sup>2</sup> A. S. Ackerman,<sup>2</sup> E. W. Eloranta,<sup>3</sup>  
and G. M. McFarquhar<sup>4</sup>

Received 24 September 2008; revised 3 March 2009; accepted 5 March 2009; published 22 May 2009.

[1] In order to evaluate possible ice formation processes in mixed phase Arctic stratocumulus, we compare measurements of radar reflectivity and Doppler velocity and lidar backscatter coefficient and circular depolarization ratio with the corresponding quantities computed from large-eddy simulations (LES). The measurements are taken from the Millimeter Cloud Radar and the Arctic High Spectral Resolution Lidar during the Mixed-Phase Arctic Cloud Experiment in October 2004. Lidar depolarization, computed from LES results including well-known ice formation and multiplication processes and measured ambient ice nuclei (IN), is near 0%, indicating negligible ice formation, whereas measured median depolarization is 84%, indicating strong ice formation, consistent with in situ aircraft measurements. Reducing ice particle fall speeds, increasing IN concentrations, or introducing a surface source of IN does not sufficiently increase the simulated depolarization values and/or results in poor agreement of other simulated parameters with the measurements. Introducing additional hypothetical ice formation processes (i.e., formation of IN from evaporating drops, freezing of evaporation drops, or droplet freezing rates per unit surface or volume) generally brings all investigated parameters into relatively close agreement with the radar and lidar measurements. These results provide additional evidence for the existence of one or more unestablished ice formation processes in Arctic stratocumulus.

**Citation:** van Dierenhoven, B., A. M. Fridlind, A. S. Ackerman, E. W. Eloranta, and G. M. McFarquhar (2009), An evaluation of ice formation in large-eddy simulations of supercooled Arctic stratocumulus using ground-based lidar and cloud radar, *J. Geophys. Res.*, 114, D10203, doi:10.1029/2008JD011198.

## 1. Introduction

[2] A better understanding of the microphysical processes of formation, growth and interaction of drops and ice particles in clouds is crucial to improve the representation of clouds in general circulation models and our understanding of their impact on Earth's climate [Intergovernmental Panel on Climate Change, 2007]. In general, many processes that control ice initiation in clouds remain poorly understood [e.g., Cantrell and Heymsfield, 2005]. In particular, for mixed phase clouds warmer than about  $-15^{\circ}\text{C}$  existing theory is unable to explain the high ice concentration often observed [e.g., Hobbs, 1969; Beard, 1992]. For these clouds homogeneous drop freezing can be ruled out as

an ice source, since the liquid water in such clouds never approaches the temperature at which pure water drops begin to freeze at substantial rates (about  $-36^{\circ}\text{C}$  for  $100\text{-}\mu\text{m}$ -diameter drops [Pruppacher and Klett, 1998]). Thus, heterogeneous ice nucleation mechanisms (i.e., ice formation promoted by aerosol impurities) are generally considered to be the main source of ice in such clouds. However, it has long been found that measured ice crystal number concentrations often exceed measured ice nucleus (IN) number concentrations by orders of magnitude [Mossop et al., 1968; Mossop, 1970, 1985; Beard, 1992]. Numerous ice multiplication processes have been identified to explain these discrepancies between measured and modeled ice number concentrations [e.g., Mossop, 1970; Pruppacher and Klett, 1998], but they are generally inadequate to explain the high ice concentrations under mixed phase conditions [Beard, 1992]. Alternative ice formation processes have also been hypothesized to explain observed ice crystal concentrations, such as formation of IN from evaporating drops [Rosinski and Morgan, 1991; Beard, 1992] or freezing of evaporating drops [Cotton and Field, 2002]. The observational evidence for such alternative ice formation processes is very sparse and detailed measurement and modeling activities are

<sup>1</sup>Center for Climate Systems Research, Columbia University, New York, New York, USA.

<sup>2</sup>NASA Goddard Institute for Space Studies, New York, New York, USA.

<sup>3</sup>Space Science and Engineering Center, University of Wisconsin–Madison, Madison, Wisconsin, USA.

<sup>4</sup>Department of Atmospheric Sciences, University of Illinois at Urbana-Champaign, Urbana, Illinois, USA.

critical to better understanding ice formation in mixed phase clouds.

[3] Here we focus on the particular case of ice formation in an observed occurrence of moderately supercooled mixed phase stratiform cloud, which is among the most common cloud type in the Arctic region [e.g., *Shupe et al.*, 2006]. Because similar such clouds are most widely found under conditions warmer than about  $-30^{\circ}\text{C}$  [e.g., *Curry et al.*, 1997; *Pinto et al.*, 2001; *Rangno and Hobbs*, 2001; *Shupe et al.*, 2006], initial ice formation proceeds heterogeneously, and cloud evolution may be sensitive to a range of factors, including cloud top radiative cooling, entrainment, mixing, temperature, surface fluxes, IN properties, ice particle properties, vapor growth rates, and feedbacks among such processes [e.g., *Pinto*, 1998; *Harrington et al.*, 1999; *Jiang et al.*, 2000; *Olsson and Harrington*, 2000; *Harrington and Olsson*, 2001; *Morrison and Pinto*, 2005; *Morrison et al.*, 2005; *Fridlind et al.*, 2007; *Prenni et al.*, 2007; *Luo et al.*, 2008; *Morrison et al.*, 2008]. A subset of past modeling studies has investigated the sources and sinks of IN when they are treated prognostically (explicitly accounting for IN depletion when ice crystals form) and generally found that the IN depletion process is rapid and can have drastic implications [*Harrington and Olsson*, 2001; *Morrison et al.*, 2005; *Fridlind et al.*, 2007; *Prenni et al.*, 2007], with the possible exception of a case in which ice formation is dominated by contact nucleation [*Morrison et al.*, 2005].

[4] Building on previous studies that use prognostic IN, *Fridlind et al.* [2007] studied ice formation in mixed phase stratocumulus by comparing liquid and ice water path, particle number concentrations and size distributions produced by large-eddy simulations (LES) that include various ice formation and multiplication schemes, with detailed in situ measurements obtained during the Mixed-Phase Arctic Cloud Experiment (M-PACE) near Barrow, Alaska. M-PACE was conducted by the US Department of Energy Atmospheric Radiation Measurement (DOE ARM) program at and around the North Slope of Alaska (NSA) from late September through late October of 2004 [*Verlinde et al.*, 2007; *McFarquhar et al.*, 2007b]. Concentrating on measurements during 9–12 October when a ubiquitous, supercooled, boundary layer stratocumulus deck occurred over the region, with cloud layer temperatures of about  $-8.5$  to  $-15.5^{\circ}\text{C}$ , *Fridlind et al.* [2007] found that ambient ice nuclei appear insufficient by a few orders of magnitude to explain observed ice, consistent with past literature. Furthermore, that study found that multiplication processes are not significant sources of ice on the basis of parameterizations from existing studies. Of the investigated alternative ice forming processes the formation of ice nuclei from drop evaporation residuals and drop freezing during evaporation were found to reproduce the M-PACE measurements best. Unfortunately, in situ measurements of ice and liquid droplet number and size distributions are subject to many uncertainties [e.g., *McFarquhar et al.*, 2007b], limiting such comparative studies.

[5] In order to obtain additional, independent clues about the viability of different ice formation processes in mixed phase clouds, this study compares measurements of the Millimeter Cloud Radar (MMCR [*Moran et al.*, 1998]) and the Arctic High Spectral Resolution Lidar (AHSRL

[*Eloranta*, 2005]) deployed at the NSA site during M-PACE with the corresponding quantities computed from the large-eddy simulations described by *Fridlind et al.* [2007]. These cloud radar and lidar observations are sensitive to cloud particle phase, number and size distributions. By comparing the radar and lidar measurements directly with their simulated counterparts, rather than comparing microphysical quantities produced by the LES with values retrieved from the measurements, possible retrieval errors are avoided. A similar general approach has been previously adopted by, e.g., *Wiedner et al.* [2004], *Marshall et al.* [2006] and *Chiriac et al.* [2006]. We compare also the radar and lidar measurements with the corresponding quantities computed directly from the in situ measurements of particle size distributions, in order to check their consistency.

[6] After describing radar and lidar measurements (section 2) and the LES, radar and lidar simulations (section 3), we present results (section 4) and conclusions (section 5).

## 2. Data

### 2.1. Millimeter Wavelength Cloud Radar

[7] The vertically pointing 35-GHz Millimeter Cloud Radar (MMCR [*Moran et al.*, 1998]) is permanently deployed at the ARM NSA site. In this paper, we use only MMCR equivalent reflectivity and mean Doppler velocity measurements (see *Battan* [1973] for definitions) obtained in the “stratus” mode, which has been optimized for observing low-level clouds [*Kollias et al.*, 2007]. Since the radar reflectivity is approximately proportional to the sixth power of the particle diameter, it is mainly sensitive to the large drops and/or ice crystals in the cloud.

[8] Figures 1a and 1b show equivalent reflectivity and Doppler velocity measurements, respectively, recorded on 9 October 2004 between 2225 and 2355 UTC. The data are averaged over 40 m in altitude and 5 s in time to achieve similar resolution among radar, lidar and model results, as discussed further below. The base of the mixed phase cloud (defined in the caption of Figure 1) is at around 700 m on average. However, this boundary is not apparent in the reflectivity, suggesting that the large droplets and/or ice crystals that are dominating the reflectivity signal have a rather even vertical distribution throughout much of the boundary layer. Alternating periods of about 2–4 min with relatively high ( $>0$  dBZ) and low reflectivities are apparent in the measurements. As can be seen from comparison with Figure 1b, these can be associated with high and low Doppler velocities, respectively.

### 2.2. Arctic High Spectral Resolution Lidar

[9] The University of Wisconsin’s Arctic High Spectral Resolution Lidar (AHSRL [*Eloranta*, 2005]) was deployed at the ARM NSA site during the M-PACE campaign. The AHSRL operates at 532 nm and can distinguish the back-scattered signal coming from air molecules and particles by utilizing their different spectral signature in the returned signal. The spectral width of Rayleigh-scattered light is increased by Doppler shifts resulting from strong thermal motions of the air molecules, while the much lower velocities of cloud particles and aerosols yield a less Doppler-broadened signal. This allows the AHSRL to directly

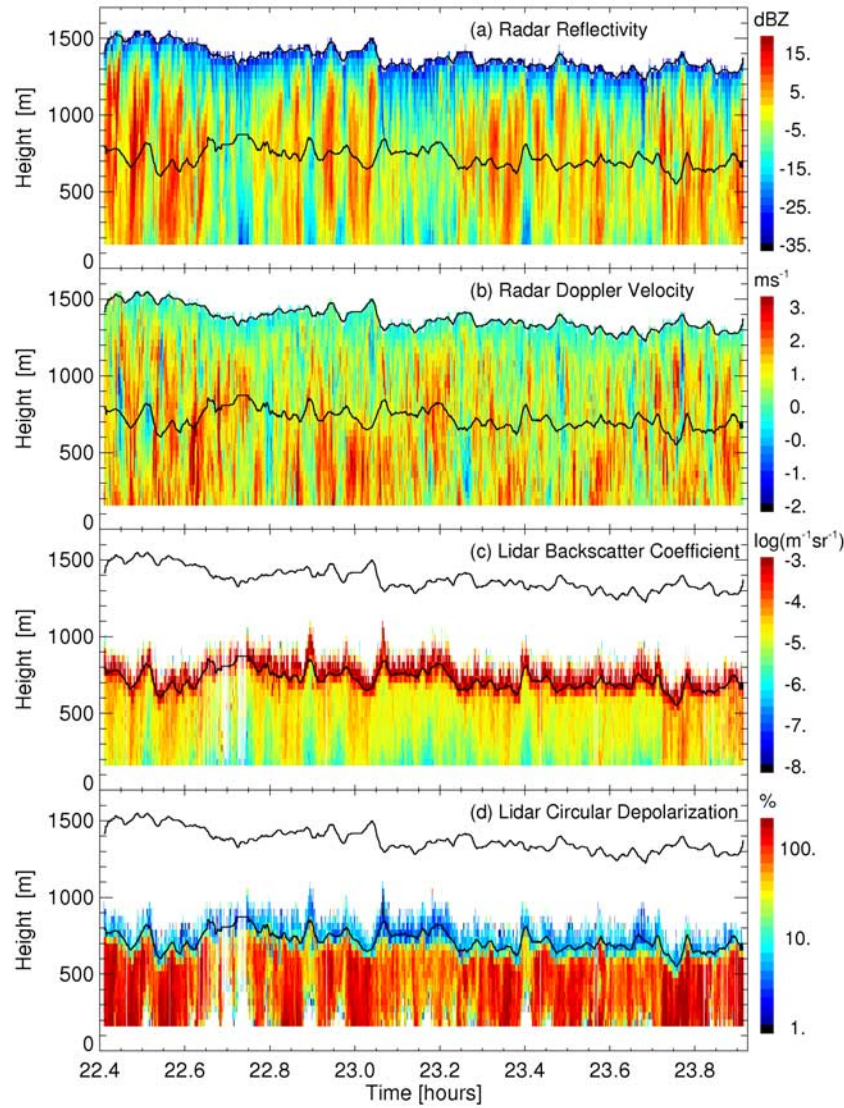


**Figure 1.** Measurements of (a) equivalent radar reflectivity, (b) radar Doppler velocity, (c) lidar backscatter coefficient, and (d) lidar circular depolarization ratio from 9 October 2004 between 2225 and 2355 UTC at the ARM NSA site near Barrow, Alaska. The top solid line indicates an estimate of the cloud top, above which the radar reflectivity is below  $-35$  dBZ. The bottom solid line indicates an estimate of the cloud base, above which the optical depth at 532 nm is larger than 1.5.

measure the backscatter coefficients  $\beta$  of the cloud particles as a function of altitude  $z$ . Here  $\beta$  is formally defined as

$$\beta(z) = \sum_{i=1}^N n_i(z) \sigma_i P_{11}(180^\circ)_i, \quad (1)$$

where  $n_i$  is the number concentration of identical particles of type  $i$ ,  $\sigma_i$  is the scattering cross section,  $P_{11}(180^\circ)_i$  is the particle single-scattering phase function in the backscattering direction, and  $N$  is the total number of particle types.

[10] The AHSRL transmits circularly polarized light and measures the altitude-dependent circular depolarization ratio  $\delta_c$  of the returned signal, defined as [Schotland *et al.*, 1971; Mishchenko and Hovenier, 1995]

$$\delta_c(z) = \frac{\beta(z) + \beta_c(z)}{\beta(z) - \beta_c(z)} \times 100\%, \quad (2)$$

where  $\beta_c$  describes the equivalent backscatter coefficient for circularly polarized light, defined similarly as in equation (1) but substituting the phase functions with the 4th diagonal of the single-scattering phase matrix of particle  $i$ ,  $P_{44}(180^\circ)_i$ . Light scattered from nonspherical particles is depolarized, while light scattered from spherical particles is not. Hence, the measured depolarization ratio provides information about the relative contributions from nonspherical (ice) and spherical (liquid) particles. Since the possible values of  $P_{44}(180^\circ)_i$  range from  $-1$  to  $1$  (indicating left- and right-handed circular polarization), and those of  $P_{11}(180^\circ)_i$  are between  $0$  and  $1$ ,  $\delta_c$  ranges from  $0\%$  to infinity. Thus,  $\delta_c$  is zero when the returned signal is not depolarized, it is  $100\%$  when the signal is completely depolarized and it is infinity when the returned signal is completely circularly polarized in the opposite direction from the emitted signal.



[11] Figures 1c and 1d show the AHSRL measurements of backscatter coefficient and circular depolarization ratio from 9 October 2004 between 2225 and 2355 UTC. (AHSRL measurements are unavailable for the first hours of 10 October that coincides with measurements taken on flight 10a of the Citation aircraft on which *Fridlind et al.* [2007] focused. However, the considered cloud layer persisted for several days under similar conditions [*McFarquhar et al.*, 2007b].) The data are averaged over 45 m in altitude and 5 s in time. Measurements are plotted up to an optical depth of 2.5, above which the signal is saturated. Since the optical depth increases rapidly above cloud base, essentially only measurements under the cloud are available. Backscatter coefficients under the cloud range from about  $10^{-6} \text{ m}^{-1} \text{ sr}^{-1}$  to  $10^{-4} \text{ m}^{-1} \text{ sr}^{-1}$  and circular depolarization ratios range from 0% to about 200%. The mean depolarization below the cloud is about 80%, indicating that many of the particles under the cloud are nonspherical ice crystals.

### 3. Simulations

#### 3.1. DHARMA Large-Eddy Simulations

[12] The simulations are made using the Distributed Hydrodynamic Aerosol-Radiation-Microphysics Application (DHARMA) code [*Ackerman et al.*, 2003], which couples models of fluid dynamics, radiative transfer, and size-resolved, mixed phase cloud microphysics. The DHARMA simulations analyzed here are described in detail by *Fridlind et al.* [2007], and we will only summarize the most important aspects here.

[13] DHARMA treats atmospheric and cloud dynamics with a large-eddy simulation code [*Stevens et al.*, 2002; *Stevens and Bretherton*, 1996] that has been modified to include a dynamic subgrid-scale turbulence model [*Kirkpatrick et al.*, 2006]. A domain of 3.2 km by 3.2 km horizontally and 2 km deep is divided into a mesh of  $64 \times 64 \times 96$ , achieving uniform grid spacings of 50 m horizontally and 20 m vertically. As discussed by *Fridlind et al.* [2007], the simulations are not able to capture mesoscale features larger than the domain size, such as the convective rolls observed in satellite imagery (approximately 10 km in diameter near Barrow). The simulations instead aim to resolve first-order coupling of cloud motions and microphysical processes such as ice formation. For the simulations shown here, all particles are treated as spheres, using 20 mass bins each to resolve aerosols (0.02–2  $\mu\text{m}$  dry diameter), liquid drops (2–2000  $\mu\text{m}$  diameter), and ice crystals (2–5000  $\mu\text{m}$  maximum diameter). The modeled particle fall speeds at each altitude are determined by the assumed particle densities, as described by *Fridlind et al.* [2007]. Thus, all particles of a given type and size have the same fall speed. Particle fall speeds could not be constrained by in situ measurements, as discussed further below. The assumed ice particle densities are consistent with semispherical, irregular and rimed particle types, which predominated during flight 10a [*McFarquhar et al.*, 2007b].

[14] All simulations are initialized with mean meteorological conditions and aerosol properties observed at Barrow by multiple instruments during the M-PACE campaign. The eight simulations investigated here include different ice nucleus (IN) concentrations, ice densities (which determine fall speeds and in turn influence vapor growth rates) and ice

nucleation processes, as discussed by *Fridlind et al.* [2007]. The first run (simulation a) includes low background IN concentrations of  $0.2 \text{ L}^{-1}$  based on in situ measurements and baseline estimates of the ice fall speeds. Here only well-known heterogeneous ice nucleation modes, i.e., contact, condensation, deposition and immersion modes [*Pruppacher and Klett*, 1998], are modeled. Standard ice multiplication processes, i.e., rime splintering, drops shattering and ice-ice collisions [*Pruppacher and Klett*, 1998], are also included. In order to increase ice formation and bring modeled and measured liquid and ice water paths (LWP and IWP, respectively) into closer agreement, the other runs include reduced ice densities and consequently reduced fall speeds (simulation b); increased background ice nucleus concentrations of  $200 \text{ L}^{-1}$  (simulation c); a surface source of ice nuclei, resulting in a constant IN concentration of  $6 \text{ L}^{-1}$  in the surface layer (simulation d); IN formation from one in every  $5 \times 10^5$  evaporating drops (simulation e); a volume-independent freezing rate of  $2 \times 10^3 \text{ s}^{-1}$  for evaporating drops (simulation f); a droplet freezing rate per unit water volume of  $10 \text{ cm}^{-3} \text{ s}^{-1}$  (simulation g); and a droplet freezing rate per unit water surface area of  $0.004 \text{ cm}^{-2} \text{ s}^{-1}$  (simulation h). The ice formation processes in simulations b–h are tuned such that the modeled LWP and IWP both agree with in situ measurements near Barrow, as detailed by *Fridlind et al.* [2007].

[15] The latter four simulations include alternative ice formation processes hypothesized in the literature, all based on the possibility that aqueous chemistry could alter organic matter inside drops to expose or form an ice nucleus or promote ice nucleation. In the case of evaporation IN (simulation e), for instance, acidification during drop evaporation could remove polymer gel coatings from organic aerosols to expose an IN which could be released when the drop evaporates [*Beard*, 1992; *Leck and Bigg*, 2005]. A similar process could also lead to direct freezing of the drops [*Bigg*, 1996; *Cantrell and Robinson*, 2006] as in simulation f. Aqueous chemistry not related to evaporation could also possibly create organic ice nuclei or surfactant films with ice nucleating properties [e.g., *Leck and Bigg*, 2005; *Zobrist et al.*, 2007], as considered in simulations g and h.

[16] Further information about the DHARMA model simulations is provided by *Fridlind et al.* [2007]. In the present study, results between 11 and 12 h of simulation time are investigated, and the vertical resolution of the simulated radar and lidar measurements is reduced by a factor of 2 (to 40 m) to obtain a similar resolution as the radar and lidar measurements.

#### 3.2. Radar Simulations

[17] Simulations of MMCR equivalent reflectivity from the DHARMA results are made using the Quickbeam software package [*Haynes et al.*, 2007]. Quickbeam calculates the scattering properties of both ice crystals and liquid droplets using Mie theory. As designed, Quickbeam requires an analytical size distribution (e.g., a lognormal, power law or monodisperse distribution) for input. To input the size-resolved particle number densities produced by the DHARMA model to Quickbeam, each size bin of both particle types is represented as a monodisperse distribution for which a hydrometeor type is defined, specifying max-

imum diameter, density and phase. This way, the only (trivial) modification to Quickbeam required was an increase of the maximum number of definable hydrometeor types. Each of the bins of the DHARMA ice crystal and liquid droplet size distributions is divided into five logarithmically equidistant bins by linearly interpolating the size distributions in order to ensure adequate sampling of scattering properties that vary rapidly with size. Rebinning uniformly across each DHARMA bin instead of linearly interpolating does not yield significantly different results. Quickbeam treats ice as “soft spheres,” in which the diameter of a given sphere is the same as the maximum dimension of the corresponding ice crystal and the effective density and index of refraction are reduced to represent a mixture of ice with air [Liu, 2004]. Multiple scattering is neglected. Errors from these approximations are not expected to significantly affect our conclusions.

[18] Assuming Rayleigh scattering, the altitude-dependent mean Doppler velocities,  $V_d$ , are approximated by

$$V_d(z) = \frac{\sum_{i=1}^N f_i V_i(z) n_i(z) D_i(z)^6}{\sum_{i=1}^N f_i n_i(z) D_i(z)^6}, \quad (3)$$

where  $n_i$ ,  $D_i$  and  $V_i$  are the number concentration, diameter and vertical velocity (including wind and particle fall speed) of particle size and type  $i$ , respectively. For ice crystals, the diameter of a melted sphere is used. The factor  $f_i$  accounts for the difference in refractive index of liquid water and ice, and is 1 for liquid droplets (by definition) and 0.197/0.93 for ice [Battán, 1973].

### 3.3. Lidar Simulations

[19] For comparison with the AHSRL measurements, backscatter cross sections and circular depolarization ratios are simulated from the DHARMA results. For liquid droplets, cross sections and scattering phase matrices are calculated using Mie theory and assuming a refractive index of 1.335. The scattering properties of the ice crystals are calculated using geometrical optics (GO [Macke et al., 1996]) and assuming a refractive index of  $1.311 - i5 \times 10^{-9}$  [Warren, 1984]. Here randomly oriented hexagonal columns are assumed with an aspect ratio of 0.6 and a maximum diameter equal to the diameter of the spherical ice particles assumed in the DHARMA model. The relation between maximum diameter and projected area of hexagonal columns with an aspect ratio of 0.6 is similar to those of rimed ice particles such as graupel [Mitchell, 1996], consistent with the assumed predominance of compact and rimed particle types in the LES calculations. Roughened column surfaces are simulated by randomly distorting the angles between the column surfaces with a maximum distortion of 10% (see Macke et al. [1996] for details). Each bin of the DHARMA ice crystal and liquid droplet size distributions is divided into ten logarithmically equidistant bins by linearly interpolating the size distributions and scattering properties are calculated for particles in each bin, again to achieve adequate estimates of properties varying rapidly with particle size. Similar results are obtained when rebinning uniformly across each DHARMA bin instead of using linear interpolation. Lidar backscatter

coefficients and depolarization ratios are then calculated using equations (1) and (2), respectively. Since the angular field of view of the AHSRL is only  $45 \mu\text{rad}$ , multiple scattering can be ignored [Eloranta, 1998] and only scattering in the exact backscatter direction is considered.

[20] Real clouds contain ice crystals of many, mostly irregular shapes and forms, with aspect ratios ranging from at least 0.4 to 0.8 for temperatures between  $-15^\circ\text{C}$  and  $-5^\circ\text{C}$  [e.g., Korolev and Isaac, 2003]. This variation is not represented in our lidar simulations. However, studies of the scattering properties of different crystal shapes, such as aggregates of columns or bullets, fractal-shaped particles and randomly distorted columns (as used here) have shown that basically all crystals with a large variation of angles have similar, featureless scattering phase functions [Macke, 1993; Macke et al., 1996; Um and McFarquhar, 2007]. Only distorted hexagonal plates can lead to significantly lower depolarization ratios, depending on their aspect ratio [Del Guasta, 2001]. However, very few plate-like particles appear in the in situ images taken during M-PACE [McFarquhar et al., 2007b]. We assume a single aspect ratio of 0.6 since the scattering properties of columns were not found to vary significantly with aspect ratio in the range of 0.4–0.8, especially with respect to the depolarization ratio [see also, e.g., Del Guasta, 2001]. Thus, although the assumption of randomly oriented hexagonal columns with an aspect ratio of 0.6 is not strictly accurate from a microphysical point of view, the resulting scattering properties are assumed to sufficiently represent those of the collection of ice crystals in the observed cloud. The variability of ice crystal scattering properties, however, is likely to be somewhat underestimated in our lidar simulations, but this limitation is not expected to significantly affect our conclusions.

[21] GO are limited by an inability to model the dependency of the phase matrix on particle size. However, Mishchenko and Macke [1999] showed that GO can be used for crystals larger than about  $20 \mu\text{m}$  at  $532 \text{ nm}$ . Because smaller ice crystals have only a minor influence on the simulations performed in this study, no corrections are applied to their phase matrices.

[22] The circular polarization element of the phase function in the backscatter direction  $P_{44}(180^\circ)$  is about 0.2 for the assumed ice crystal properties. This leads to a maximum depolarization of about 150%. In the AHSRL measurements shown in Figure 1 depolarization ratios up to 200% are observed. These high depolarization ratios could originate from regions with an increased amount of highly irregular ice as depolarization increases with increasing particle distortion. Particle orientation can also lead to high depolarization ratios [Del Guasta et al., 2006]. Mishchenko and Sassen [1998] further showed that extremely small ice crystals with sizes on the order of  $1 \mu\text{m}$  can strongly depolarize. However, there is no evidence of sufficiently high concentrations of such small particles in the investigated clouds to explain the high depolarization measurements. We also note that the GO code used here calculates the phase function in discrete  $0.5^\circ$  scattering angle bins, which can lead to a slight underestimation of  $P_{44}(180^\circ)$  and hence the depolarization [Macke et al., 1996]. Since these

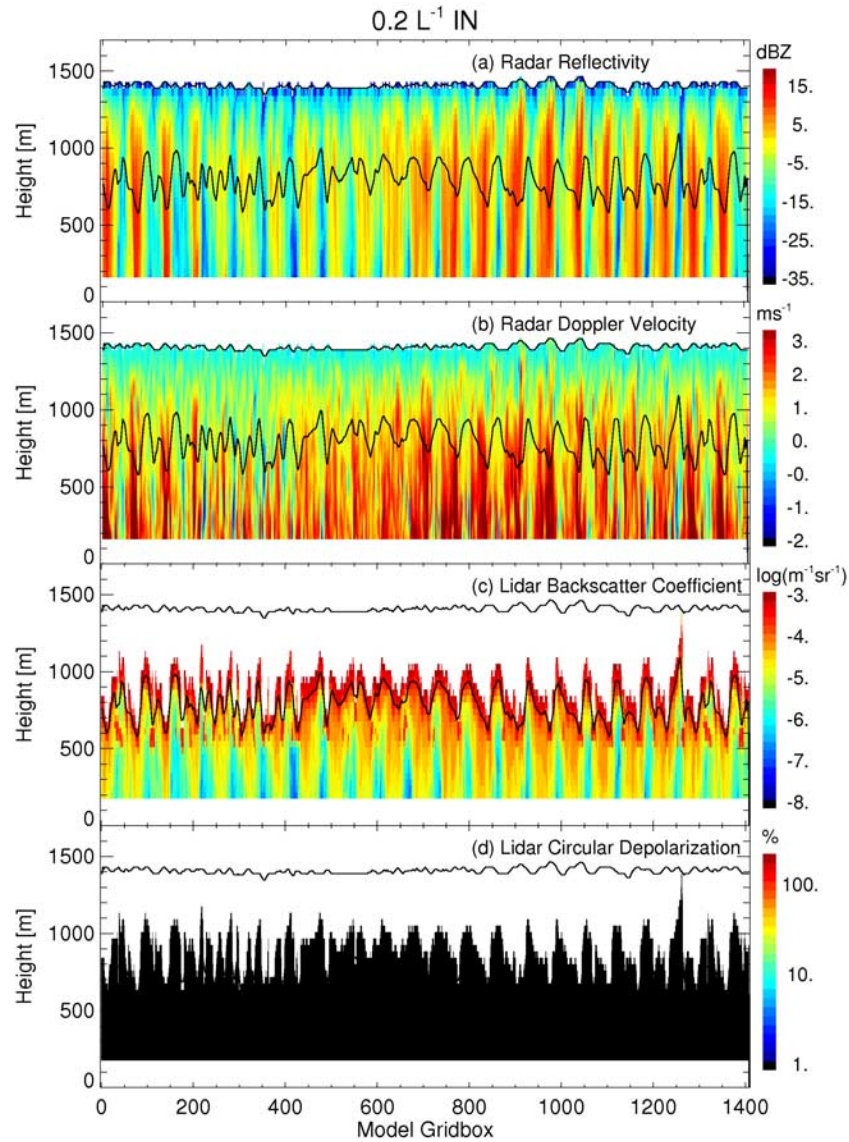


**Figure 2.** Same as Figure 1 but for simulated measurements based on the large-eddy simulation including only the standard heterogeneous ice nucleation and multiplication mechanisms and IN concentrations of  $0.2 \text{ L}^{-1}$  (simulation a as described in section 3.1). For the sake of visual comparison with Figure 1, here we horizontally cycle through one time slice of the model grid, visiting about one third of the entire model domain (see text, section 4.1). Each model grid box is 50 m in width.

differences do not significantly impact our conclusions, no correction is made.

## 4. Results

### 4.1. Simulated Measurements for DHARMA Results

[23] Figure 2 demonstrates the simulated radar and lidar measurements for the DHARMA simulation including only the standard heterogeneous ice nucleation and multiplication mechanisms and IN concentrations of  $0.2 \text{ L}^{-1}$  (simulation a as described in section 3.1). Similarly, Figure 3 demonstrates the simulated measurements for the DHARMA simulation that includes evaporation IN, leading to a significantly greater ice content (simulation e). For the purposes of demonstrating the simplest visual comparison with the measurements, in Figures 2 and 3 we horizontally cycle through

one time slice of the model grid, taking 1 step to the north after every 20 steps to the east. Thus time series with a similar temporal resolution as the lidar and radar measurements are mimicked with model spatial resolution by exploiting the Taylor hypothesis [Taylor, 1922], transforming space to time using the average, steady wind speed of about 13 m/s and the wind direction. We note that the average ratio of the turbulent velocity scale to the mean wind is about 0.05 in the boundary layer, well within the regime where Taylor's hypothesis applies. We stress that the statistical analysis in this study is not based on these visual comparisons but rather on the statistical comparisons described later.

[24] The reflectivity and backscatter coefficient simulations for both cases show some similar general features seen in the measurements in Figure 1. Alternating cells of high and low reflectivity and backscatter coefficients have roughly



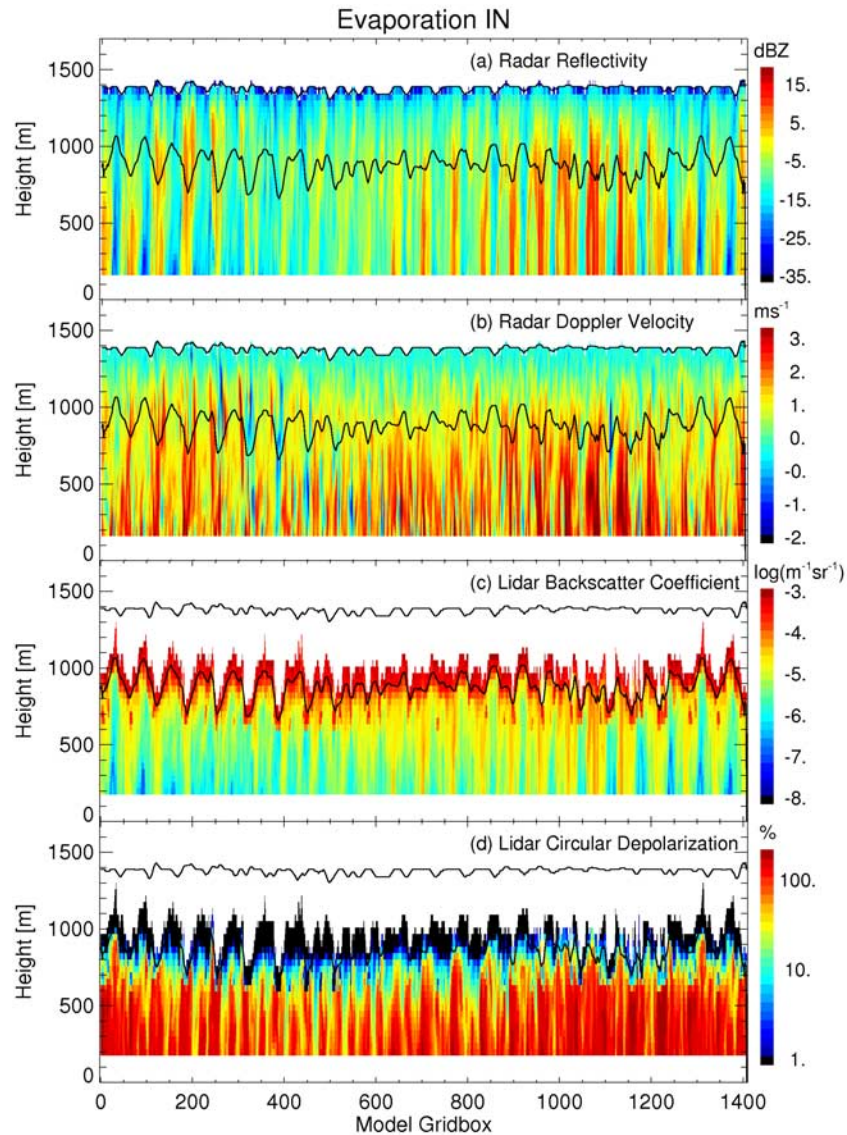


**Figure 3.** Same as Figure 2 but for simulated measurements based on the large-eddy simulation including evaporation IN (simulation e as described in section 3.1).

similar widths and magnitudes as those seen in the measurements. Furthermore, reflectivities appear similar under and in the cloud, as is the case in the measurements. The most striking difference is between the measured depolarization (Figure 1d) and the simulated values for the case with low IN concentrations (Figure 2d). The simulated depolarization values near zero show that ice formation for this simulation is negligible. The depolarization values simulated by the model including evaporation IN bear greater resemblance to the measured values. This will be discussed further below. For both simulations, the cloud base is generally higher than that in the measurements. Furthermore, the variation in cloud base height is significantly greater than observed, especially in the simulations including only the low background IN concentrations (Figure 2). Overall, the similarity of Figures 2 and 3 to Figure 1 suggests that the bulk features of the cloud and boundary layer dynamics during M-PACE are reproduced to first order by the model. Similar fields for the remaining simulations (simulations b–d and f–h de-

scribed in section 3.1) can be found as auxiliary material to this paper (Figures S1–S6).<sup>1</sup>

[25] To statistically compare the simulations with the measurements, histograms of the simulations and measurements between 400 m and 600 m (under the cloud) are constructed. We focus on the area below cloud because all measured lidar and radar quantities are available there. To take into account the oscillations in LWP and IWP in the model results on about a half hourly time scale, as shown by *Fridlind et al.* [2007], three fields output during the last hour of each simulation (at 1100, 1130 and 1200 simulation time) are randomly sampled to obtain the same number of data points as in the measurements. To check the sensitivity of our results to the number of fields sampled within the last hour of simulation, we also produced histograms for a subset of our simulations (simulations a, b, and e as

<sup>1</sup>Auxiliary materials are available in the HTML. doi:10.1029/2008JD011198.

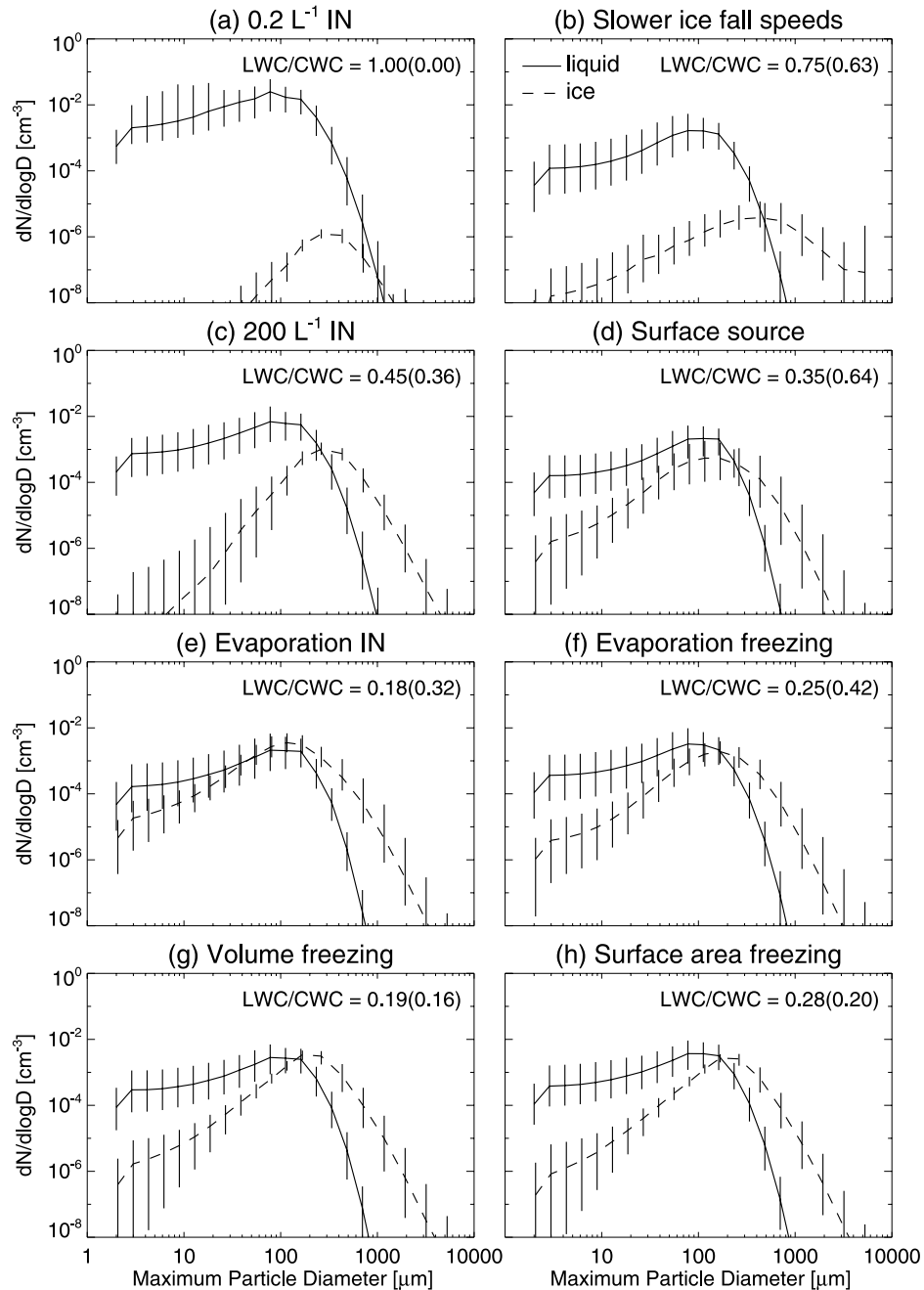


**Figure 4.** Median values of the sampled size distributions of liquid drops (solid line) and ice crystals (dashed line) predicted below cloud base in the DHARMA simulations. Vertical lines represent the 25th to 75th percentile ranges. (a) Simulation a, (b) simulation b, (c) simulation c, (d) simulation d, (e) simulation e, (f) simulation f, (g) simulation g, and (h) simulation h, as described in section 3.1. The median and IQR of the LWC fraction (LWC/CWC) for each simulation is given in the top right corner of the corresponding plot.

described in section 3.1), sampling from fields produced at every 5 min simulations time. Similar results were found (not shown). The median and 25th and 75th percentiles of the sampled size distributions of drops and ice are shown in Figure 4. Also shown in Figure 4 are the median and interquartile ranges (IQR) of the liquid water content (LWC) fraction, defined as the LWC divided by the total condensed water content (CWC). The size distributions show a large variation between simulations, especially with

respect to ice. The LWC fraction also varies greatly between simulations. Aside we note that slight accumulation of ice crystal numbers in the largest size bin appears in the simulation with reduced ice fall speeds (Figure 4b). The simulation was repeated with four additional size bins, but no significant effect on the radar and lidar simulations was found (not shown).

[26] Figure 5 shows histograms of measured and simulated reflectivities below cloud. For the case with low IN



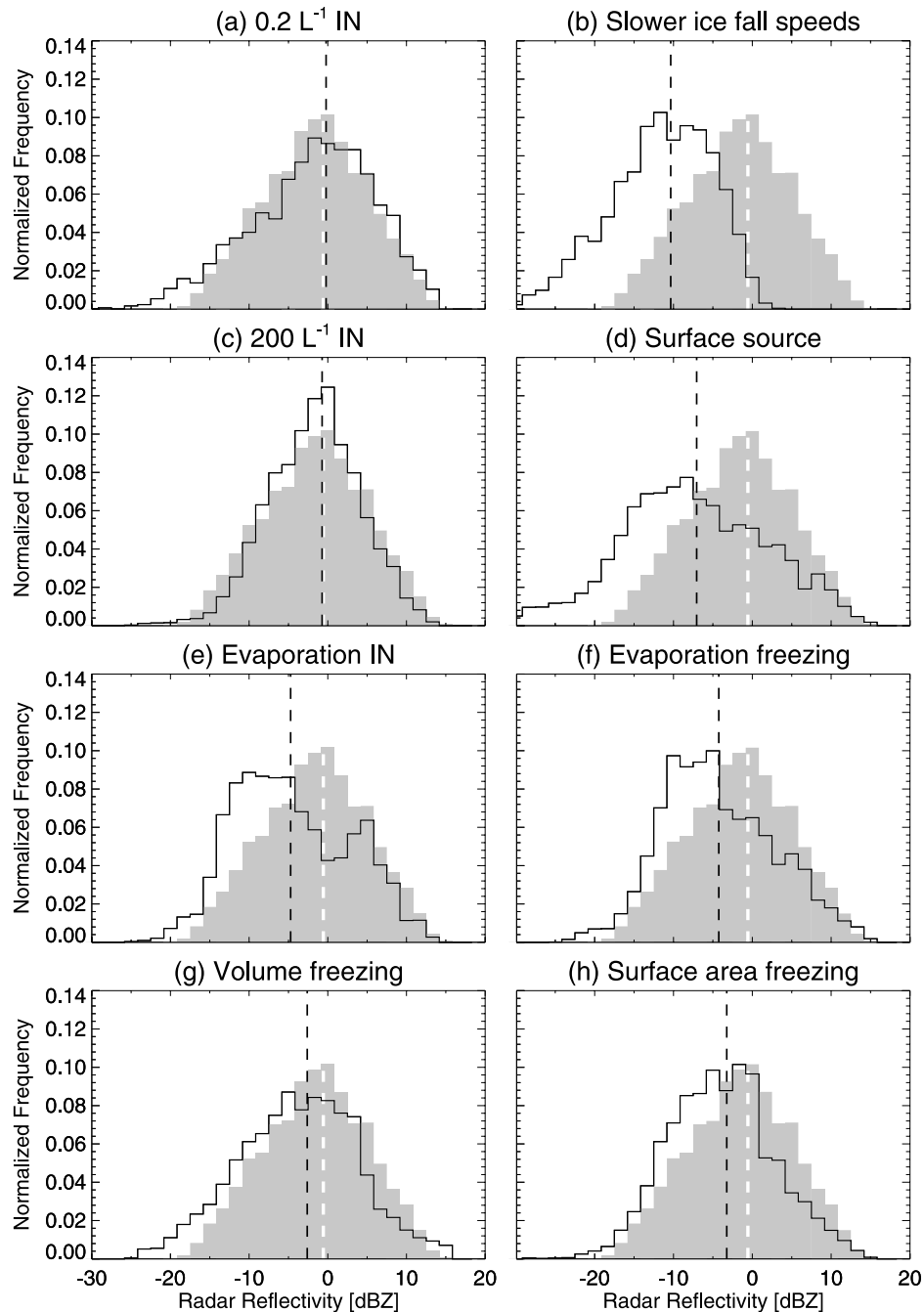


**Figure 5.** Measured equivalent radar reflectivities (shaded area; dashed white line indicates median value) and simulated equivalent radar reflectivities (solid lines; dashed black line indicates median value) below cloud base. (a) Simulation a, (b) simulation b, (c) simulation c, (d) simulation d, (e) simulation e, (f) simulation f, (g) simulation g, and (h) simulation h, as described in section 3.1.

concentrations (Figure 5a), the distribution of reflectivities under the cloud is very similar to those in the measurements. The median reflectivity below cloud is  $-0.22$  dBZ, which is only about  $0.35$  dBZ higher than the median of the measured values. In this simulation, generally the high reflectivity values ( $>0$  dBZ) are produced by a relatively high concentration of large drops also apparent in Figure 4, while signals below  $0$  dBZ are obtained in regions with predominately smaller drops. As can be seen from the size distributions and the LWC fraction given in Figure 4a,

essentially no ice is formed in this simulation, although in situ measurements indicated significant ice water paths of about  $12$  g/m<sup>2</sup> on average as discussed by Fridlind *et al.* [2007]. Furthermore, the LWP in this simulation is almost twice that measured [Fridlind *et al.*, 2007]. In an effort to bring the modeled LWP and IWP within the range of observed levels the ice fall speeds are decreased (Figure 5b). However, this change leads to a low median reflectivity of  $-10.4$  dBZ. These low reflectivities are attributable to the fact that only relatively few large ice crystals are produced in this simu-

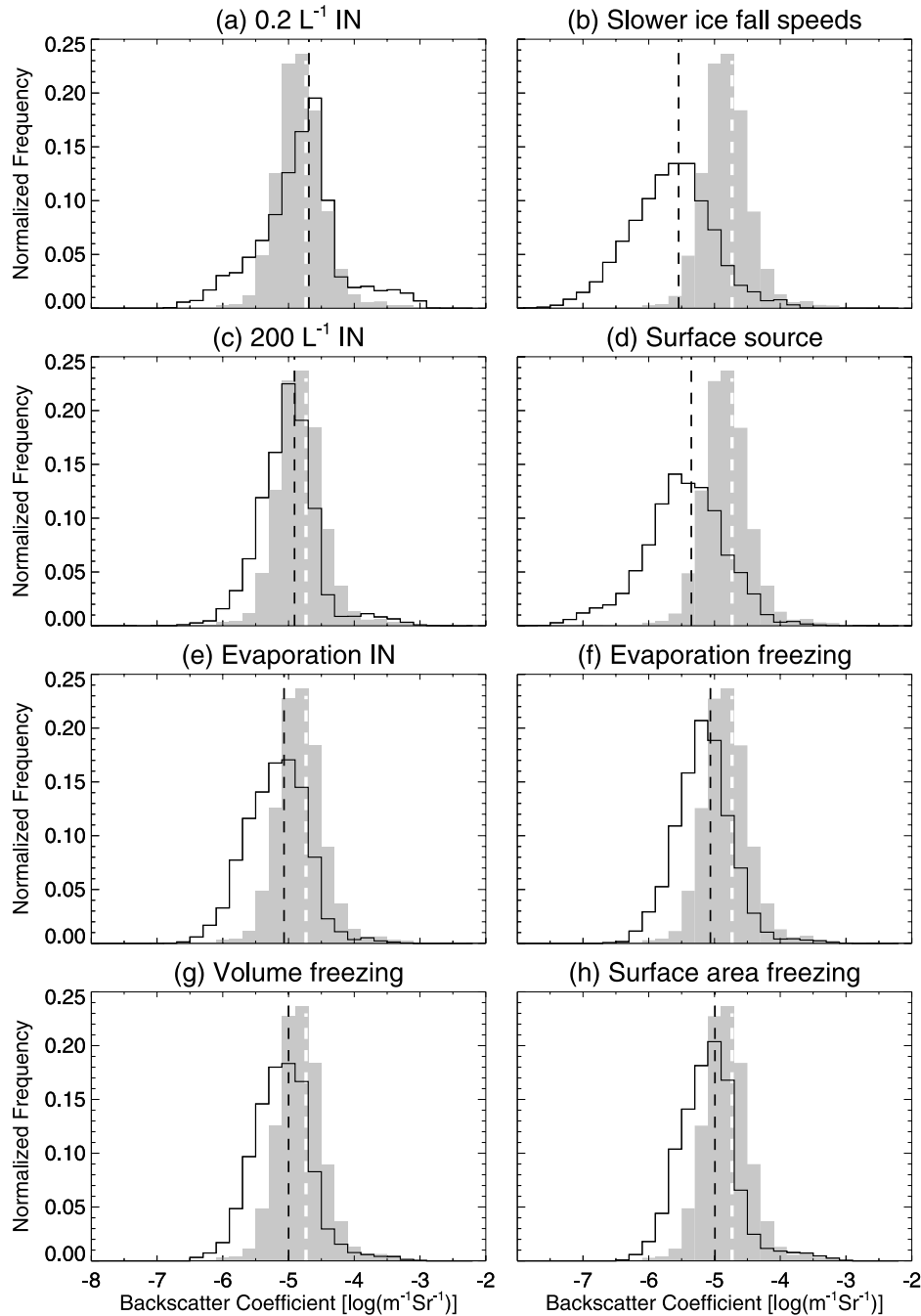


**Figure 6.** Same as Figure 5 but for lidar backscatter coefficients below cloud base.

lation, while the liquid drop concentrations are significantly diminished, as apparent from the size distributions shown in Figure 4b. When the background IN concentration is increased to  $200 \text{ L}^{-1}$  (Figure 5c), the reflectivity median and its distribution are similar to those of the measurements. Here, the concentration of ice crystals is higher (see Figure 4c) than that for the previous cases and ice contributes more to high dBZ values. When a surface source of IN is introduced (Figure 5d), the reflectivity median is significantly lower than the measurements and its distribution is significantly broader. As can be seen in Figure 4d, a fair amount of ice is produced in this simulation. However, the LWC fraction and its IQR are relatively high, indicating

strong variability between regions with low and high ice content, relative to liquid water. This variability explains the broad distribution of reflectivities, where high values are primarily attributable to ice crystals, while the lower values are attributable to water droplets.

[27] Figure 5 also shows histograms of reflectivities for the models including the alternative ice formation processes (see section 3.1), i.e., evaporation IN (Figure 5e), freezing of evaporating drops (Figure 5f), freezing rates per unit volume (Figure 5g), and freezing rate per unit surface (Figure 5h). For the case with evaporation IN (Figure 5e), the median values are  $-4.8 \text{ dBZ}$ , which is about  $4.2 \text{ dBZ}$  lower than that of the measurements. The distribution is also

slightly bimodal. A similar distribution is seen for the case that includes freezing of evaporating drops (Figure 5f). Again the high and low reflectivities of the bimodal distribution are primarily attributable to ice crystals and water droplets, respectively. However, the distribution is narrower than that for the simulation including the surface source (Figure 5d), because the median and IQR of the LWC fraction is significantly lower for these cases. The results for the simulations including a freezing rate per unit volume (Figure 5g) and including a freezing rate per unit surface area (Figure 5h) both show slightly lower median reflectivities than the measurements. The reflectivities are more evenly distributed in the latter two cases, consistent with the relatively low IQR of the LWC fraction given in Figures 4g and 4h.

[28] Analogous size distributions and reflectivity histograms for measured and simulated radar reflectivity in the cloud (between 900 m and 1100 m) can be found in the auxiliary material (Figures S7 and S8, respectively). Overall, similar variations are found within and under the cloud, although the agreement between observations and model results appears to be slightly better within the cloud. Histograms of the measured and simulated Doppler velocities in and under the cloud can also be found in the auxiliary material (Figures S9 and S10). Generally, the Doppler velocities agree well with the measurements and do not vary significantly between model simulations. These results will be discussed further in section 4.3.

[29] Figure 6 shows the histograms of simulated and measured lidar backscatter coefficients under the cloud. For the case with low IN concentrations (Figure 6a), the median value of  $-4.7 \log(\text{m}^{-1} \text{sr}^{-1})$  (the notation  $\beta = x \log(\text{m}^{-1} \text{sr}^{-1})$ , equivalent to  $\log_{10}(\beta) = x$ , where  $\beta$  is in units of  $\text{m}^{-1} \text{sr}^{-1}$ , is used throughout) agrees with the measurements. A significant wing toward high values is seen in this case, which is less pronounced in the measurements and the other simulations. This wing is related to the strong variability in cloud base height for the case with low IN concentrations, as discussed above. At a few locations the simulated cloud base falls within our vertical sampling range (400–600 m), leading to high backscatter coefficients. When the sampling range is restricted to 400–500 m, the wing is significantly reduced for this case as well as for the other simulations and the measurements (not shown). Otherwise the histograms of the lidar backscatter coefficients do not significantly change when the vertical sampling range is restricted, nor do the histograms of other observables (not shown). The histogram of backscatter coefficients for the case with low IN concentrations also shows an overestimation of low backscatter coefficient values, indicating that at some locations the total weighted cross-sectional area of the drops and ice crystals in the simulations is too low. The cases with lower ice fall speeds (Figure 6b) and a surface source of IN (Figure 6d) show small median backscatter coefficients of  $-5.5 \log(\text{m}^{-1} \text{sr}^{-1})$  and  $-5.3 \log(\text{m}^{-1} \text{sr}^{-1})$ , respectively, indicating that the modeled total weighted cross-sectional area of the drops and ice crystals is significantly too low compared with the measurements. This shortcoming is consistent with the lower peak values of the liquid and ice size distributions for these two cases, compared with the other cases, as shown in Figure 4. The shape of the distribution of backscatter

coefficients for the case with high IN concentrations (Figure 6c) and the alternative ice formation processes (Figures 6e–6h) are similar and agree fairly well with the measurements, although distributions are generally broader than the measurements with median values that are about  $0.3 \log(\text{m}^{-1} \text{sr}^{-1})$  lower than the measurements. Again this bias indicates that the total weighted cross-sectional area of the drops and ice crystals predicted by the model is generally somewhat too low under cloud base.

[30] Of all parameters we have investigated, by far the greatest distinction between the model runs is seen in the depolarization values, as shown in Figure 7. The depolarization values in the measurements are distributed between 0% and 200% with a median of 84%. For the case with low IN (Figure 7a), however, no depolarization is obtained. This reflects the fact that negligible ice is present in this simulation. Higher depolarization values are obtained in the cases with slower ice fall speeds (Figure 7b), high IN concentrations (Figure 7c), and a surface source of IN (Figure 7d), although still many more depolarization values close to zero are simulated than are observed. The poor agreement of these simulated depolarization distributions with the measurements suggests that too little ice relative to the amount of liquid water is present at many locations below the cloud in these simulations, consistent with their relatively high median LWC fractions shown in Figure 4. For the cases with alternative ice production processes (Figures 7e–7h) the simulated depolarization values agree better with the measurements. In the simulation including evaporation IN (Figure 7e) the median depolarization value is 81%. However, the distribution appears to be bimodal with peaks around 100% and 20%. Apparently this simulation produces some areas with too much water and other areas with too much ice compared to the measurements. This situation is even more pronounced in the results with freezing of evaporating droplets (Figure 7f). The distributions of depolarization ratios in the cases of freezing rates per unit volume (Figure 7g) and surface area (Figure 7h) show a better resemblance to that of the measurements, which is consistent with the lower IQR of the LWC fraction for these cases compared to the previous ones, as seen in Figure 4. However, the median value for the case with freezing rates per surface area is somewhat low at 60%. Note that because of limitations in the GO simulations of the scattering phase matrix, discussed in section 3.3, the maximum depolarization value in the simulation is 150%, while higher values are seen in the measurements. Although it is not clear which attributes of particles (i.e., size, shape, etc.) are responsible for these high depolarization values, inclusion of such particle attributes in the simulations could lead to broader distributions and higher median values. These results are discussed further in section 4.3.

## 4.2. Simulated Measurements Using In Situ Measured Size Distributions

[31] Size distributions of the hydrometeors in and under the cloud were measured in situ by multiple instruments on the Citation aircraft during M-PACE, as detailed by *McFarquhar et al.* [2007b]. *Fridlind et al.* [2007] compared the measured size distributions with simulated values and found the best agreement for simulations including a surface source (simulation d), evaporation IN (simulation e) and



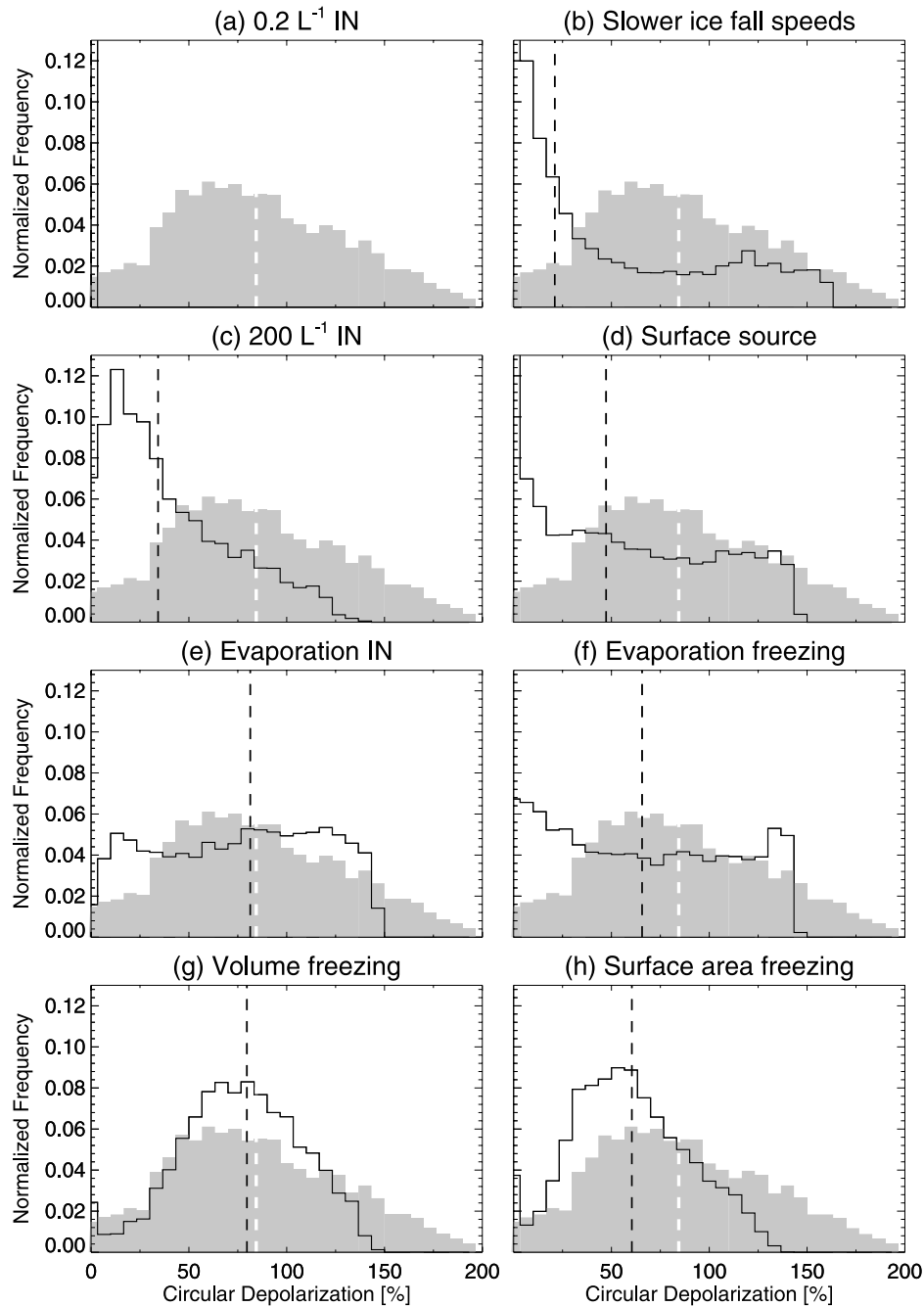


**Figure 7.** Same as Figure 5 but for lidar circular depolarization ratio below cloud base.

evaporation of freezing droplets (simulation f). However, aircraft hydrometeor size distribution measurements in the presence of ice are subject to many uncertainties, such as difficulty in classifying particle shapes, the potential ice shattering on protruding components of probes, and poor sampling statistics of larger particles [McFarquhar *et al.*, 2007b]. Here we compare lidar and radar measurements under the cloud with the simulated measurements based on the aircraft data in order to check their consistency.

[32] We use size distributions measured by three different instruments: a forward scattering spectrometer probe (FSSP, 3–53  $\mu\text{m}$  maximum particle dimension), a two-dimensional cloud probe (2DC, 54–4000  $\mu\text{m}$ ) and a high-volume

precipitation sampler (HVPS, 400–40000  $\mu\text{m}$ ). FSSP and 2DC measurements were obtained on flights 9 and 10a (referred to as 9a and 9b, respectively, by Verlinde *et al.* [2007]) on 9 and 10 October 2004, respectively. Unfortunately, HVPS measurements are not available for these flights. Instead, the 2DC size distributions were extrapolated to larger sizes using fits based on 2DC and HVPS data from 12 October, as discussed by McFarquhar *et al.* [2007b]. We also note that for ice clouds, the ability of the FSSP to measure ice crystal size distributions has not been well established [Gardiner and Hallett, 1985; Field *et al.*, 2003; McFarquhar *et al.*, 2007a] and there is some evidence that large ice crystals shatter on the protruding airflow shrouds

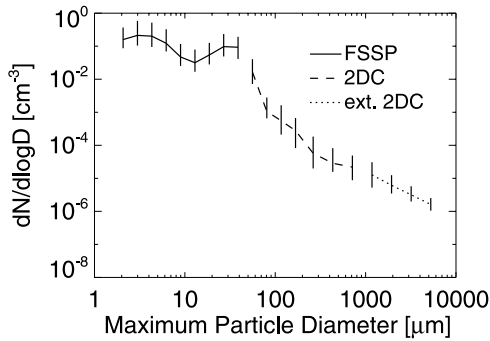


**Figure 8.** Median values of the 179 in situ measured particle size distributions used in section 4.2. Solid and dashed lines indicate the parts of the size distributions measured by the FSSP and the 2DC, respectively. The dotted line indicates the extrapolated 2DC data (see section 4.2). Vertical lines indicate the 25th to 75th percentile ranges.

of the FSSP, generating artificially high counts of small crystals. Further, there are large uncertainties in the concentrations of particles smaller than  $125\ \mu\text{m}$  measured by the 2DC in light of previous studies suggesting that the depth of field and hence sample area for such small particles are poorly defined with the 2DC [Baumgardner and Korolev, 1997; Strapp et al., 2001].

[33] To obtain continuous size distributions, data from the FSSP ( $3\text{--}53\ \mu\text{m}$ ), 2DC ( $54\text{--}960\ \mu\text{m}$ ) and the extended 2DC data ( $1000\text{--}40000\ \mu\text{m}$ ) are combined. The size distributions are subsequently interpolated onto the same size grid as used in the radar and lidar simulations discussed in sections 3.2 and 3.3, respectively. We assume all particles to be ice crystals, since 90% of the measured size distributions under the cloud were reported to be in the ice phase. The remaining 10% were identified as mixed phase, but separate size distributions for liquid and ice particles are not available. In total 179 size distribution measurements are used here. The median and 25th to 75th percentile ranges of the size distributions are shown in Figure 8.

[34] Figure 9 shows the histogram of the reflectivities under the cloud based on the aircraft measurements. The median reflectivity is only about 1 dBZ higher than that of the radar measurements, although the distribution is narrower. Note that the reflectivity signal is dominated by the large ice crystals (with maximum dimensions greater than about  $1000\ \mu\text{m}$ ), which were not measured in these flights but were obtained by extrapolating the 2DC data to larger sizes. In the same way that McFarquhar et al. [2007b] showed that the distributions of effective radius were much narrower for time periods when averaged HVPS distributions were used compared to actual HVPS measurements, it can be shown that the extrapolation based on average HVPS measurements underestimates the spatial variation of number concentrations, which might explain the narrow distribution of reflectivities seen in Figure 9 relative to the observations. Note that these possible errors do not significantly affect the backscatter coefficients and depolarization values.

[35] The backscatter coefficients calculated from the aircraft measurements, shown in Figure 10a, agree fairly

well with the measured values. The median backscatter coefficient is only about  $0.3\ \log(\text{m}^{-1}\ \text{sr}^{-1})$  lower than that of the measurements. The distribution resembles those from the simulations including the alternative ice formation processes shown in Figures 6e–6g. The depolarization values shown in Figure 10c, however, do not agree with the measurements. Only depolarization ratios around 150% are obtained, which is the maximum possible value for the simulations (see section 3.3). This narrow distribution of depolarization ratios may result in part from the absence of spatial/temporal variation of ice crystal shapes in our simulated measurements, as discussed in section 3.3. However, the possible variation of depolarization ratios attributable to varying ice crystal shape is small [e.g., Mishchenko and Sassen, 1998], and is insufficient to explain the large range of measured depolarization ratios. Moreover, the depolarization ratios for the DHARMA model simulations including the alternative ice formation processes (Figures 7e–7g) do show broad depolarization distributions similar to the measurements, despite the lack of ice crystal shape variation. The agreement in these cases results from a small, spatially varying amount of liquid water (with an average LWC of  $\sim 0.004\ \text{g m}^{-3}$ ) being present under the cloud in addition to the ice. By replacing a small amount of small ice (maximum dimension  $< 80\ \mu\text{m}$ ) with liquid water droplets, a broader distribution of depolarization ratios is obtained in the simulation from the aircraft measurements. Since the mass width of the size bins for all hydrometeors are equal, we simply subtract a fraction of the mass of ice smaller than  $< 80\ \mu\text{m}$  and add it to the corresponding bins for the water drops, obtaining a specified LWC. A constant LWC of  $0.003\ \text{g m}^{-3}$  is enough to obtain a depolarization distribution more similar to the measurements, as seen in Figure 10d. This replacement also brings the backscatter coefficients into slightly better agreement with the measurements as shown in Figure 10b. Furthermore, the addition of such a small amount of liquid water has no effect on the calculated radar reflectivity (not shown). Note that the LWC added to explain the measured depolarization distributions is below the  $0.02\ \text{g m}^{-3}$  LWC detection limit of the King probe [Heymsfield and

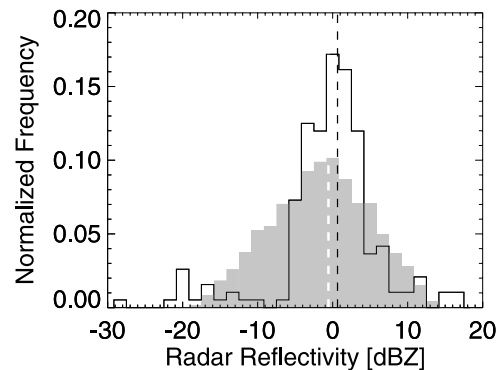


**Figure 9.** Measured equivalent radar reflectivities below cloud base (shaded area; dashed white line indicates median value) and corresponding simulated equivalent radar reflectivities (solid lines; dashed black line indicates median value) based on the Citation aircraft in situ measurements of ice size distributions.

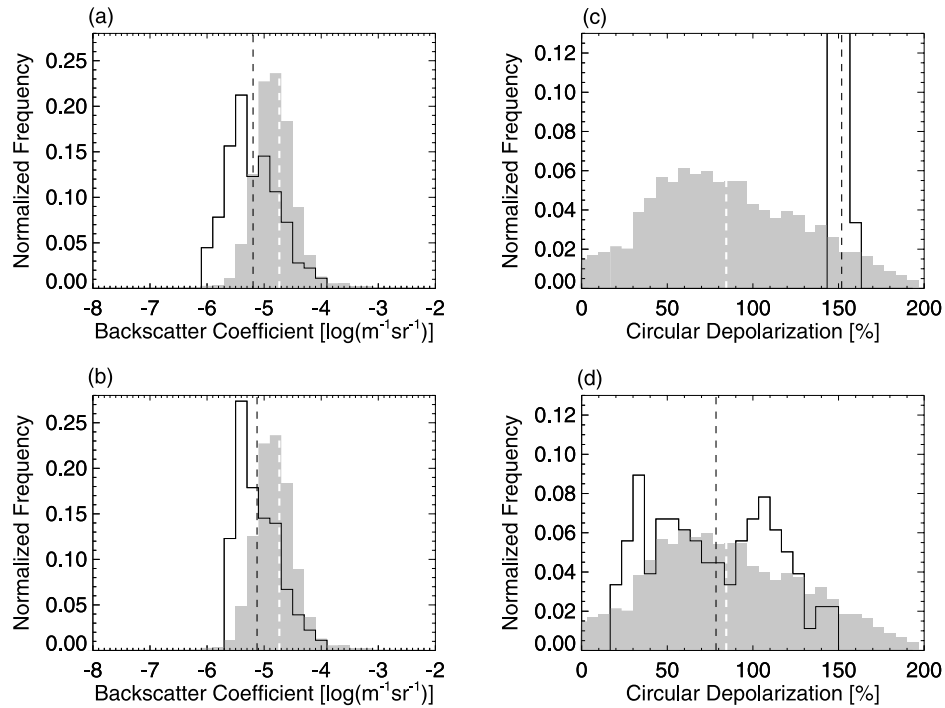


**Figure 10.** Same as Figure 9 but for the (a and b) lidar backscatter coefficients and (c and d) circular depolarization. For Figures 10a and 10c, all particles are assumed to be ice. For Figures 10b and 10d, a small amount of small ice ( $D < 80 \mu\text{m}$ ) is replaced by liquid drops, comprising a LWC of  $0.003 \text{ g m}^{-3}$ .

Miloshevich, 1989] and the  $0.007 \pm 0.01 \text{ g m}^{-3}$  detection limit of the Rosemount Icing Detector [Cober *et al.*, 2001] that were flown during M-PACE [McFarquhar *et al.*, 2007b]. CPI images also show liquid drops below cloud base [e.g., McFarquhar *et al.*, 2007b], consistent with the fact that clouds with such high LWP and low droplet number concentrations are associated with significant drizzle rates [Comstock *et al.*, 2004]. Lidar depolarization measurements have been successfully used to discriminate particle habits or orientation in cold cirrus clouds [e.g., Del Guasta, 2001; Chepfer *et al.*, 2005], in which liquid drops can be excluded and the presence of various pristine and irregular crystals shapes can lead to a significant variation in

depolarization. However, the high sensitivity of the depolarization ratio to small amounts of liquid water implies that care must be taken when using depolarization measurements to discriminate particle habits or orientation in clouds that may include supercooled water [e.g., Del Guasta *et al.*, 2006].

[36] As discussed above, the ability of instruments such as the FSSP and 2DC to measure the number distributions of small ice crystals is not well established. To test the sensitivity of our results to small ice crystals, we repeat the simulated lidar and radar measurements based on the in situ size distributions but remove the small ice crystals (with maximum dimensions up to  $200 \mu\text{m}$ ) and redistribute their

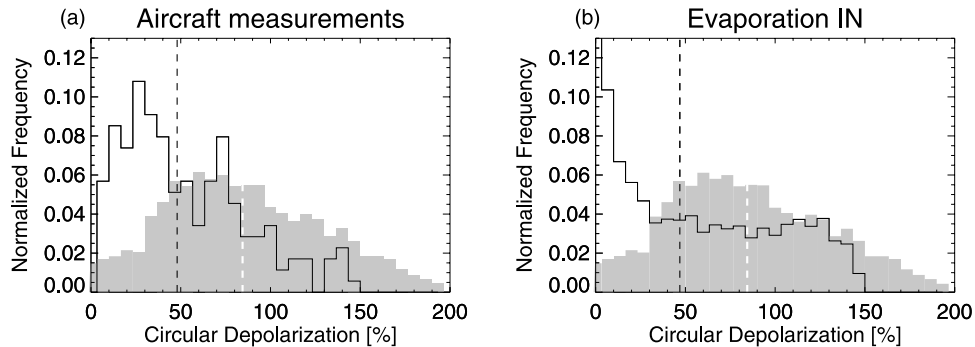


**Figure 11.** Simulated lidar circular depolarization based on (a) aircraft in situ measurements (solid line, compare with Figure 10d) and (b) LES results including evaporation IN (solid line, compare with Figure 7e), where ice crystals with maximum dimensions smaller than  $200 \mu\text{m}$  are removed and their mass is redistributed to the larger size bins. Shaded area shows the measured lidar depolarization. A small amount of liquid water is added to the aircraft measurements leading to a LWC of  $0.003 \text{ g m}^{-3}$ , as discussed in section 4.2.



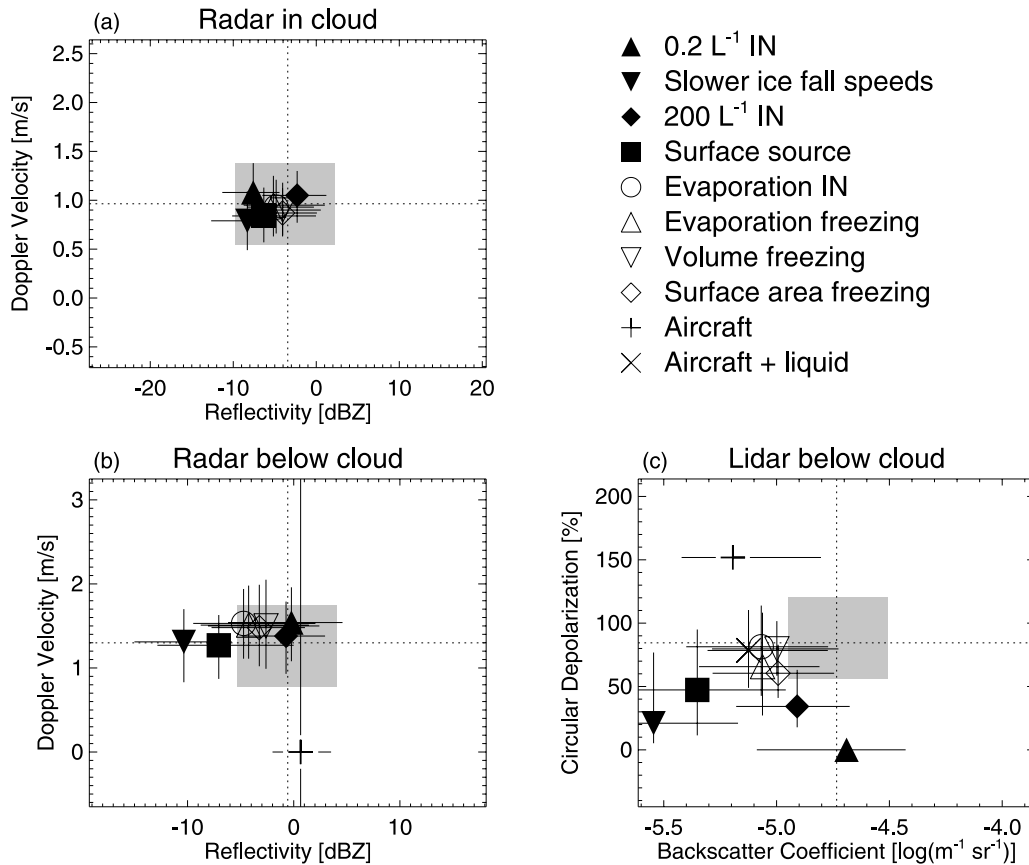


**Figure 12.** Median simulated equivalent radar reflectivity versus Doppler velocity (a) in cloud and (b) below cloud and (c) median simulated lidar backscatter coefficient versus depolarization below cloud. Solid lines through the symbols represent the corresponding first through third quartile ranges. The intersections of the dotted lines indicate the measured median values. The gray box spans the first through third quartile ranges of measured values. Closed and open symbols indicate different large-eddy simulations described in section 3.1. Pluses (Figures 12b and 12c) and the cross (Figure 12c) are for the simulations based on the in situ measurements assuming all ice hydrometeors and replacing some ice with liquid droplets, respectively, as described in section 4.2.

mass uniformly into the large size bins. The radar simulations are not significantly affected by redistributing the small ice crystals since this only changes the concentration of large ice crystals slightly (not shown). The median of simulated lidar backscatter coefficients (not shown) also decreases only slightly by about  $0.2 \log(\text{m}^{-1} \text{sr}^{-1})$ . However, the lidar depolarization does show a significant effect as seen by comparing Figure 11b with Figure 10d. Removing the small ice crystals leads to a decrease of the median depolarization to about 50%, but this decrease can be compensated by decreasing the small amount of added liquid water by about half (not shown). Thus, the uncertainty in the amount of liquid water in the simulations based on in situ measurements hampers any conclusion to be made here about the existence of small ice based on the lidar depolarization. In another approach to investigate the presence of such small ice crystals, we repeat this procedure for the large-eddy simulation that includes evaporation IN (simulation e). As can be seen from comparing Figure 11b with Figure 7e, removing the small ice crystals from the LES results leads to an increase in the number of depolarization values near 0%. Apparently in some areas removing

the small ice (maximum dimension  $<200 \mu\text{m}$ ) leaves mostly liquid water, leading to low depolarization values. A similar result is obtained for the simulation including other alternative ice formation processes (simulations e–f, not shown). Thus, the sensitivity of the LES results to the removal of small ice suggests that a significant amount of small ice could possibly be present in the observed cloud deck.

[37] Overall, we conclude that, given the forward model uncertainties, our instrument simulations based on the in situ measured size distributions are largely consistent with the radar and lidar measurements under cloud base.

#### 4.3. Synopsis

[38] To summarize our findings, Figure 12 shows the median values of simulated radar reflectivity and Doppler velocity in and below the cloud, and of simulated lidar backscatter and depolarization below the cloud. The first through third quartile ranges of simulated parameters are represented by the solid lines drawn through the corresponding symbols. The difference of these quartiles is the IQR. The center (intersects of dotted lines) of each

panel in Figure 12 shows the median values of the corresponding measured parameters, and the grey boxes span their first through third quartile ranges. Simulations that reproduce the measurements well are identified by a significant overlap between first through third quartile ranges of measured and simulated values for all parameters. Overall, radar measurements in the cloud are reproduced similarly well by all simulations, while somewhat more variation is seen in the radar simulations under the cloud. Most distinction between simulations, however, is seen in the lidar results.

[39] The simulations including only the background (low) IN concentrations (simulation a, see section 3.1) reproduce the radar measurements in and below cloud and lidar backscatter coefficient under the cloud fairly well. The match to these measurements is remarkable since essentially no ice is produced in this simulation, as is clearly seen in the poor comparison of measured and simulated lidar depolarization. The absence of depolarization in this simulation, however, shows that the conditions during M-PACE are not well reproduced by the model simulation including only background (low) IN concentrations and standard ice nucleation and multiplication processes.

[40] Somewhat more ice (by number and mass) is produced by the simulation including lower ice densities and consequently lower ice fall speeds (simulation b). However, the simulated depolarization is still significantly lower than the measured value. Moreover, the simulated reflectivity and backscatter coefficient under the cloud are clearly too low. Also the IQR of the backscatter coefficient is much larger than that of the measurements. These disagreements indicate that the simulated particle size distributions in this case are inconsistent with the measurements.

[41] When the IN concentration is increased by several orders of magnitude greater than measured (simulation c), the radar measurements in and below the cloud and the backscatter coefficient under the cloud are well reproduced. The lidar depolarization, however, is still significantly lower than measured. Moreover, as pointed out by *Fridlind et al.* [2007], the large amounts of IN used in this simulation seem unlikely to have gone undetected by the CFDC instrument used during M-PACE [*McFarquhar et al.*, 2007b].

[42] Introducing a surface source of IN brings the simulated depolarization somewhat closer to the measurements. The backscatter coefficients under the cloud, however, are too low compared to the measurements, while the IQR of the backscatter coefficient is significantly larger, again indicating unrealistic particle size distributions.

[43] The radar and lidar measurements are best reproduced by the simulations including alternative processes for ice formation (simulations e–h, open symbols in Figure 12). Especially the lidar depolarization measurements are better reproduced compared to the previous simulations. These simulations appear in clusters in Figure 12 and we are unable to distinguish which may be more realistic. However, the better agreement for the case with a tuned freezing rate per unit volume (simulation g) with the measured distributions of radar reflectivity and lidar depolarization in particular, seen in Figures 5 and 7 hints that ice formation processes which favor a more uniform horizontal distribution of the LWC fraction might be more realistic.

[44] Simulations based on the aircraft in situ measurements (plus sign and crosses in Figure 12) compare reasonably well with the measurements. The median radar reflectivity is similar to the measurements but the IQR is considerably lower. These differences could be explained by errors in the distribution of large ice crystals caused by extrapolating 2DC data using average HVPS data from a different flight and date. Note that computation of Doppler velocities using the in situ measurements is not possible, indicated by a value of  $0 \text{ m s}^{-1}$  with infinite IQR. The simulated backscatter coefficients compare reasonably well with the measurements. The depolarization values, however, are much too high with a low IQR when all particles are assumed to be ice. Replacing a small quantity of the small ice with liquid droplets brings the depolarization into good agreement with the measurements.

## 5. Conclusions

[45] We find that direct comparison of measured equivalent radar reflectivity, radar Doppler velocity, lidar backscatter coefficient and especially lidar circular depolarization with the corresponding simulated quantities based on large-eddy simulations gives valuable clues about ice formation processes in mixed phase stratiform clouds observed during M-PACE: (1) Radar reflectivity helps to identify those simulations that produce too few large ice crystals or liquid drops below cloud base. (2) Radar Doppler velocities, while not varying much between different simulations, suggest that modeled particle fall speeds (a model parameter that could not be constrained with any in situ measurements) are generally realistic. (3) Lidar backscatter helps to identify those simulations for which the weighted cross-sectional area of the cloud particles under cloud base is unrealistic. (4) Lidar depolarization provides a relatively powerful means of identifying the simulations with realistic relative amounts of liquid water and ice crystals under cloud base.

[46] The results in this study are best viewed in combination with the work presented by *Fridlind et al.* [2007]. That study concluded that IWP, LWP and cloud particle size distributions measured during M-PACE are best reproduced by the simulations when formation of IN from evaporating drops or drop freezing during evaporation are included. Of these two processes, formation of IN from evaporating drops could better explain the persistence of mixed phase conditions in simulations of the less vigorous stratus observed during the Beaufort Arctic Storms Experiment [*Curry et al.*, 1997]. However, such studies are hampered by uncertainties associated with in situ measurements of ice and liquid particle size distributions. Taking into account the possible errors in the simulations and other considerations discussed here, we conclude that the simulations are consistent with the radar and lidar measurements taken during M-PACE only when alternative ice formation processes, namely formation of IN from evaporation drops, freezing of evaporating drops or applying arbitrary droplet freezing rates per unit surface or volume, are included. The present work adds some independent evidence for the existence of one or more unestablished ice formation processes in Arctic stratocumulus (for the conditions such as found

during M-PACE) to the evidence from studies based on in situ measurements [e.g., *Rangno and Hobbs*, 2001].

[47] **Acknowledgments.** This material is based upon work supported by NASA under grant 06-EOS/06-100 issued through the Science Mission Directorate, Earth Science Division, and by the Department of Energy under Interagency Agreement DE-AI02-06ER64173 issued through the Office of Science, Office of Biological and Environmental Research. M-PACE in situ data and MCCR data were obtained from the Atmospheric Radiation Measurement (ARM) Program sponsored by the U.S. Department of Energy, Office of Science, Office of Biological and Environmental Research, Environmental Sciences Division. AHSRL data were obtained from the University of Wisconsin. Computational resources were provided by the NASA Advanced Supercomputing Division through the NASA High-End Computing Program. We thank Michael Mishchenko for valuable conversations. We are grateful for contributions from three anonymous reviewers.

## References

- Ackerman, A. S., O. B. Toon, D. E. Stevens, and J. A. Coakley Jr. (2003), Enhancement of cloud cover and suppression of nocturnal drizzle in stratocumulus polluted by haze, *Geophys. Res. Lett.*, **30**(7), 1381, doi:10.1029/2002GL016634.
- Battian, L. J. (1973), *Radar Observations of the Atmosphere*, Univ. of Chicago Press, Chicago, Ill.
- Baumgardner, D., and A. Korolev (1997), Airspeed corrections for optical array probe sample volumes, *J. Atmos. Oceanic Technol.*, **14**, 1224–1229, doi:10.1175/1520-0426(1997)014.
- Beard, K. V. (1992), Ice initiation in warm-base convective clouds: An assessment of microphysical mechanisms, *Atmos. Res.*, **28**, 125–152.
- Bigg, E. K. (1996), Ice forming nuclei in the high Arctic, *Tellus, Ser. B*, **48**, 223–233, doi:10.1034/j.1600-0889.1996.t01-1-00007.x.
- Cantrell, W., and A. Heymsfield (2005), Production of ice in tropospheric clouds: A review, *Bull. Am. Meteorol. Soc.*, **86**, 795–807.
- Cantrell, W., and C. Robinson (2006), Heterogeneous freezing of ammonium sulfate and sodium chloride solutions by long chain alcohols, *Geophys. Res. Lett.*, **33**, L07802, doi:10.1029/2005GL024945.
- Chepfer, H., V. Noel, P. Minnis, D. Baumgardner, L. Nguyen, G. Raga, M. J. McGill, and P. Yang (2005), Particle habit in tropical ice clouds during CRYSTAL-FACE: Comparison of two remote sensing techniques with in situ observations, *J. Geophys. Res.*, **110**, D16204, doi:10.1029/2004JD005455.
- Chiriac, M., R. Vautard, H. Chepfer, M. Haefelin, J. Dudhia, Y. Wanherdrick, Y. Morille, and A. Protat (2006), The ability of MM5 to simulate ice clouds: Systematic comparison between simulated and measured fluxes and lidar/radar profiles at the SARTA Atmospheric Observatory, *Mon. Weather Rev.*, **134**, 897–918, doi:10.1175/MWR3102.1.
- Cober, S. G., G. A. Isaac, and A. V. Korolev (2001), Assessing the Rosemount icing detector with in situ measurements, *J. Atmos. Oceanic Technol.*, **18**, 515–528, doi:10.1175/1520-0426(2001)018.
- Comstock, K. K., R. Wood, S. E. Yuter, and C. S. Bretherton (2004), Reflectivity and rain rate in and below drizzling stratocumulus, *Q. J. R. Meteorol. Soc.*, **130**, 2891–2918, doi:10.1256/qj.03.187.
- Cotton, R. J., and P. R. Field (2002), Ice nucleation characteristics of an isolated wave cloud, *Q. J. R. Meteorol. Soc.*, **128**, 2417–2437.
- Curry, J. A., J. O. Pinto, T. Benner, and M. Tschudi (1997), Evolution of the cloudy boundary layer during the autumnal freezing of the Beaufort Sea, *J. Geophys. Res.*, **102**, 13,851–13,860, doi:10.1029/96JD03089.
- Del Guasta, M. (2001), Simulation of lidar returns from pristine and deformed hexagonal ice prisms in cold cirrus by means of “face tracing”, *J. Geophys. Res.*, **106**, 12,589–12,602.
- Del Guasta, M., E. Vallar, O. Riviere, F. Castagnoli, V. Venturi, and M. Morandi (2006), Use of polarimetric lidar for the study of oriented ice plates in clouds, *Appl. Opt.*, **45**, 4878–4887.
- Eloranta, E. E. (2005), High spectral resolution lidar, in *Lidar: Range-Resolved Optical Remote Sensing of the Atmosphere*, edited by C. Weitkamp, pp. 143–163, Springer, New York.
- Eloranta, E. W. (1998), Practical model for the calculation of multiply scattered lidar returns, **37**, 2464–2472, doi:10.1364/AO.37.002464.
- Field, P. R., R. Wood, P. R. A. Brown, P. H. Kaye, E. Hirst, R. Greenaway, and J. A. Smith (2003), Ice particle interarrival times measured with a fast FSSP, *J. Atmos. Oceanic Technol.*, **20**, 249–261, doi:10.1175/1520-0426(2003)020.
- Fridlind, A. M., A. S. Ackerman, G. McFarquhar, G. Zhang, M. R. Poellot, P. J. DeMott, A. J. Prenni, and A. J. Heymsfield (2007), Ice properties of single-layer stratocumulus during the Mixed-Phase Arctic Cloud Experiment: 2. Model results, *J. Geophys. Res.*, **112**, D24202, doi:10.1029/2007JD008646.
- Gardiner, B. A., and J. Hallett (1985), Degradation of in-cloud forward scattering spectrometer probe measurements in the presence of ice particles, *J. Atmos. Oceanic Technol.*, **2**, 171–180, doi:10.1175/1520-0426(1985)002.
- Harrington, J. Y., and P. Q. Olsson (2001), On the potential influence of ice nuclei on surface-forced marine stratocumulus cloud dynamics, *J. Geophys. Res.*, **106**, 27,473–27,484.
- Harrington, J. Y., T. Reisin, W. R. Cotton, and S. M. Kreidenweis (1999), Cloud resolving simulations of Arctic stratus: Part II: Transition-season clouds, *Atmos. Res.*, **51**, 45–75.
- Haynes, J., R. Marchand, Z. Luo, A. Bodas-Salcedo, and G. Stephens (2007), A multi-purpose radar simulation package: QuickBeam, *Bull. Am. Meteorol. Soc.*, **88**, 1723–1727.
- Heymsfield, A. J., and L. M. Miloshevich (1989), Evaluation of liquid water measuring instruments in cold clouds sampled during FIRE, *J. Atmos. Oceanic Technol.*, **6**, 378–388, doi:10.1175/1520-0426(1989)006.
- Hobbs, P. V. (1969), Ice multiplication in clouds, *J. Atmos. Sci.*, **26**, 315–318.
- Intergovernmental Panel on Climate Change (2007), *Climate Change 2007: The Physical Science Basis—Contribution of Working Group I to the Fourth Assessment Report of the Intergovernmental Panel on Climate Change*, Cambridge Univ. Press, New York.
- Jiang, H., W. R. Cotton, J. O. Pinto, J. A. Curry, and M. J. Weisbluth (2000), Cloud resolving simulations of mixed-phase Arctic stratus observed during BASE: Sensitivity to concentration of ice crystals and large-scale heat and moisture advection, *J. Atmos. Sci.*, **57**, 2105–2117.
- Kirkpatrick, M. P., A. S. Ackerman, D. E. Stevens, and N. N. Mansour (2006), On the application of the dynamic Smagorinsky model to large-eddy simulations of the cloud-topped atmospheric boundary layer, *J. Atmos. Sci.*, **63**, 526–546.
- Kollias, P., E. E. Clothiaux, M. A. Miller, E. P. Luke, K. L. Johnson, K. P. Moran, K. B. Widener, and B. A. Albrecht (2007), The Atmospheric Radiation Measurement Program cloud profiling radars: Second-generation sampling strategies, processing, and cloud data products, *J. Atmos. Oceanic Technol.*, **24**, 1199–1214, doi:10.1175/JTECH2033.1.
- Korolev, A., and G. Isaac (2003), Roundness and aspect ratio of particles in ice clouds, *J. Atmos. Sci.*, **60**, 1795–1808.
- Leck, C., and E. K. Bigg (2005), Source and evolution of the marine aerosol: A new perspective, *Geophys. Res. Lett.*, **32**, L19803, doi:10.1029/2005GL023651.
- Liu, G. (2004), Approximation of single scattering properties of ice and snow particles for high microwave frequencies, *J. Atmos. Sci.*, **61**, 2441–2456.
- Luo, Y., K.-M. Xu, H. Morrison, and G. McFarquhar (2008), Arctic mixed-phase clouds simulated by a cloud-resolving model: Comparison with ARM observations and sensitivity to microphysics parameterizations, *J. Atmos. Sci.*, **65**, 1285–1303, doi:10.1175/2007JAS2467.1.
- Macke, A. (1993), Scattering of light by polyhedral ice crystals, *Appl. Opt.*, **32**, 2780–2788.
- Macke, A., J. Mueller, and E. Raschke (1996), Single scattering properties of atmospheric ice crystals, *J. Atmos. Sci.*, **53**, 2813–2825.
- Marsham, J. H., S. Dobbie, and R. J. Hogan (2006), Evaluation of a large-eddy model simulation of a mixed-phase altocumulus cloud using microwave radiometer, lidar and Doppler radar data, *Q. J. R. Meteorol. Soc.*, **132**, 1693–1715.
- McFarquhar, G. M., J. Um, M. Freer, D. Baumgardner, G. L. Kok, and G. Mace (2007a), Importance of small ice crystals to cirrus properties: Observations from the Tropical Warm Pool International Cloud Experiment (TWP-ICE), *Geophys. Res. Lett.*, **34**, L13803, doi:10.1029/2007GL029865.
- McFarquhar, G. M., G. Zhang, M. R. Poellot, G. L. Kok, R. McCoy, T. Tooman, A. Fridlind, and A. J. Heymsfield (2007b), Ice properties of single-layer stratocumulus during the Mixed-Phase Arctic Cloud Experiment: 1. Observations, *J. Geophys. Res.*, **112**, D24201, doi:10.1029/2007JD008633.
- Mishchenko, M. I., and J. W. Hovenier (1995), Depolarization of light backscattered by randomly oriented nonspherical particles, *Opt. Lett.*, **20**, 1356–1358.
- Mishchenko, M. I., and A. Macke (1999), How big should hexagonal ice crystals be to produce halos?, *Appl. Opt.*, **38**, 1626–1629.
- Mishchenko, M. I., and K. Sassen (1998), Depolarization of lidar returns by small ice crystals: An application to contrails, *Geophys. Res. Lett.*, **25**, 309–312, doi:10.1029/97GL03764.
- Mitchell, D. L. (1996), Use of mass- and area-dimensional power laws for determining precipitation particle terminal velocities, *J. Atmos. Sci.*, **53**, 1710–1723, doi:10.1175/1520-0469(1996)053.
- Moran, K. P., B. E. Martner, M. J. Post, R. A. Kropfli, D. C. Welsh, and K. B. Widener (1998), An unattended cloud-profiling radar for use in climate research, *Bull. Am. Meteorol. Soc.*, **79**, 443–455.
- Morrison, H., and J. O. Pinto (2005), Mesoscale modeling of springtime Arctic mixed-phase stratiform clouds using a new two-moment bulk microphysics scheme, *J. Atmos. Sci.*, **62**, 3683–3704.



- Morrison, H., M. D. Shupe, J. O. Pinto, and J. A. Curry (2005), Possible roles of ice nucleation mode and ice nuclei depletion in the extended lifetime of Arctic mixed-phase clouds, *Geophys. Res. Lett.*, **32**, L18801, doi:10.1029/2005GL023614.
- Morrison, H., J. O. Pinto, J. A. Curry, and G. M. McFarquhar (2008), Sensitivity of modeled Arctic mixed-phase stratocumulus to cloud condensation and ice nuclei over regionally varying surface conditions, *J. Geophys. Res.*, **113**, D05203, doi:10.1029/2007JD008729.
- Mossop, S. C. (1970), Concentrations of ice crystals in clouds, *Bull. Am. Meteorol. Soc.*, **51**, 474–480.
- Mossop, S. C. (1985), The origin and concentration of ice crystals in clouds, *Bull. Am. Meteorol. Soc.*, **66**, 264–273.
- Mossop, S. C., R. E. Ruskin, and K. J. Heffernan (1968), Glaciation of a cumulus at approximately  $-4^{\circ}\text{C}$ , *J. Atmos. Sci.*, **25**, 889–899.
- Olsson, P. Q., and J. Y. Harrington (2000), Dynamics and Energetics of the cloudy boundary layer in simulations of off-ice flow in the marginal ice zone, *J. Geophys. Res.*, **105**, 11,889–11,899.
- Pinto, J. O. (1998), Autumnal mixed-phase cloudy boundary layers in the Arctic, *J. Atmos. Sci.*, **55**, 2016–2038.
- Pinto, J. O., J. A. Curry, and J. M. Intrieri (2001), Cloud-aerosol interactions during autumn over Beaufort Sea, *J. Geophys. Res.*, **106**, 15,077–15,097.
- Prenni, A. J., J. Y. Harrington, M. Tjernström, P. J. DeMott, A. Avramov, C. N. Long, S. M. Kreidenweis, P. Q. Olsson, and J. Verlinde (2007), Can ice-nucleating aerosols affect Arctic seasonal climate?, *Bull. Am. Meteorol. Soc.*, **88**, 541–550, doi:10.1175/BAMS-88-4-541.
- Pruppacher, H. R., and J. D. Klett (1998), *Microphysics of Clouds and Precipitation*, 2nd ed., Kluwer Acad, Dordrecht, Netherlands.
- Rangno, A. L., and P. V. Hobbs (2001), Ice particles in stratiform clouds in the Arctic and possible mechanisms for the production of high ice concentrations, *J. Geophys. Res.*, **106**, 15,065–15,076, doi:10.1029/2000JD900286.
- Rosinski, J., and G. P. Morgan (1991), Cloud condensation nuclei as a source of ice-forming nuclei in clouds, *J. Aerosol Sci.*, **22**, 123–133.
- Schotland, R. M., K. Sassen, and R. Stone (1971), Observations by lidar of linear depolarization ratios for hydrometeors, *J. Appl. Meteorol.*, **10**, 1011–1017.
- Shupe, M. D., S. Y. Matrosov, and T. Uttal (2006), Arctic mixed-phase cloud properties derived from surface-based sensors at SHEBA, *J. Atmos. Sci.*, **63**, 697–711.
- Stevens, D. E., and C. S. Bretherton (1996), A forward-in-time advection scheme and adaptive multilevel flow solver for nearly incompressible atmospheric flow, *J. Comput. Phys.*, **129**, 284–295.
- Stevens, D. E., A. S. Ackerman, and C. S. Bretherton (2002), Effects of domain size and numerical resolution on the simulation of shallow cumulus convection, *J. Atmos. Sci.*, **59**, 3285–3301.
- Strapp, J. W., F. Albers, A. Reuter, A. V. Korolev, U. Maixner, E. Rashke, and Z. Vukovic (2001), Laboratory measurements of the response of a PMS OAP-2DC, *J. Atmos. Oceanic Technol.*, **18**, 1150–1170, doi:10.1175/1520-0426(2001)018.
- Taylor, G. I. (1922), Diffusion by continuous movements, *Proc. London Math. Soc.*, **A20**, 196–212.
- Um, J., and G. M. McFarquhar (2007), Single-scattering properties of aggregates of bullet rosettes in cirrus, *J. Appl. Meteorol. Climatol.*, **46**, 757–775, doi:10.1175/JAM2501.1.
- Verlinde, J., et al. (2007), The Mixed-Phase Arctic Cloud Experiment, *Bull. Am. Meteorol. Soc.*, **88**, 205–221, doi:10.1175/BAMS-88-2-205.
- Warren, S. G. (1984), Optical constants of ice from the ultraviolet to the microwave, *Appl. Opt.*, **23**(8), 1206–1225.
- Wiedner, M., C. Prigent, J. R. Pardo, O. Nuissier, J.-P. Chaboureaud, J.-P. Pinty, and P. Mascart (2004), Modeling of passive microwave responses in convective situations using output from mesoscale models: Comparison with TRMM/TMI satellite observations, *J. Geophys. Res.*, **109**, D06214, doi:10.1029/2003JD004280.
- Zobrist, B., T. Koop, B. P. Luo, C. Marcolli, and T. Peter (2007), Heterogeneous ice nucleation rate coefficient of water droplets coated by a nonadecanol monolayer, *J. Phys. Chem.*, **111**, 2149–2155.

---

A. S. Ackerman, A. M. Fridlind, and B. van Dierenhoven, NASA Goddard Institute for Space Studies, 2880 Broadway, New York, NY 10025, USA. (bvandierenhoven@giss.nasa.gov)

E. W. Eloranta, Space Science and Engineering Center, University of Wisconsin–Madison, 1225 West Dayton Street, Madison, WI 53706, USA.

G. M. McFarquhar, Department of Atmospheric Sciences, University of Illinois at Urbana-Champaign, 105 South Gregory Street, Urbana, IL 61801, USA.